

**Spin glass behavior in the disordered half-Heusler compound IrMnGa**

Johannes Kroder,<sup>1</sup> Kaustuv Manna,<sup>1</sup> Dominik Kriegner,<sup>1</sup> A. S. Sukhanov,<sup>1,2</sup> Enke Liu,<sup>1</sup> Horst Borrmann,<sup>1</sup> Andreas Hoser,<sup>3</sup> Johannes Gooth,<sup>1</sup> Walter Schnelle,<sup>1</sup> Dmytro S. Inosov,<sup>2</sup> Gerhard H. Fecher,<sup>1,\*</sup> and Claudia Felser<sup>1</sup>

<sup>1</sup>Max-Planck-Institut für Chemische Physik fester Stoffe, 01187 Dresden, Germany

<sup>2</sup>Institut für Festkörper- und Materialphysik, Technische Universität Dresden, 01062 Dresden, Germany

<sup>3</sup>Helmholtz-Zentrum Berlin für Materialien und Energie, 14109 Berlin, Germany



(Received 19 February 2019; published 13 May 2019)

Heusler compounds with heavy elements often display noncollinear magnetic structures, which can lead to phenomena such as the topological Hall effect. In this study, we report the structural, magnetic, electronic, and transport properties of IrMnGa. X-ray and neutron diffraction experiments reveal that the compound crystallizes in the cubic half-Heusler space group 216 with *Y*-type disorder. Manganese occupies two nonequivalent positions, causing frustration and preventing long-range magnetic order. As a consequence, a spin glass state is observed below 74 K. The spin glass state exhibits a pronounced bifurcation between field-cooled and zero-field-cooled magnetization curves, shifted hysteresis loops after field cooling, magnetic relaxation, the memory effect, absence of magnetic-ordering peaks in neutron diffraction, and a sharp cusp of the ac susceptibility. The shift of the freezing temperature as a function of ac frequency is well described by the Vogel-Fulcher law and by a critical-scaling approach indicating that IrMnGa is a canonical spin glass. Magnetotransport (including the anomalous Hall effect) and heat capacity were also investigated.

DOI: [10.1103/PhysRevB.99.174410](https://doi.org/10.1103/PhysRevB.99.174410)

**I. INTRODUCTION**

Noncollinear magnetic structures lead to interesting phenomena such as the anomalous Hall effect in antiferromagnets [1,2] or the topological Hall effect [3–5]. Such noncollinear ordering is often observed in materials with heavy atoms because the sizable spin-orbit coupling tends to cant the magnetic moments [6]. In the class of Heusler alloys for example, Mn<sub>2</sub>RhSn, Pt<sub>2</sub>MnGa, Mn<sub>1.4</sub>(Pt,Pd)Ga, and CuMnSb show noncollinear ordering [7–11].

In this study, the half-Heusler system IrMnGa is investigated. The compound crystallizes in the ordinary face-centered-cubic space group 216 but with pronounced atomic disorder whose type has not been completely understood to date [12,13]. Based on limited magnetometry data, the magnetic order was suggested to be antiferromagnetic [13] but not studied in detail. Two questions arise here, namely, what is the type of chemical disorder and to which magnetic order does it lead?

By employing neutron and x-ray diffraction experiments, we demonstrate that a *Y*-type chemical disorder is the most likely one. The high degree of chemical disorder, involving manganese atoms on two nonequivalent sites, prevents the establishment of long-range magnetic order. In fact, magnetic measurements reveal a spin glass transition at low temperatures.

Spin glasses are magnetically frustrated systems that originate from disorder and competing exchange interactions [14–16]. Below the freezing temperature, the moments arrange collectively in a random noncoplanar manner with

only short-range order. This highly metastable ordering is very sensitive to the history of applied magnetic field and temperature, which leads to phenomena such as an irreversibility between field-cooled and zero-field-cooled magnetization as well as to magnetic relaxation processes. A useful technique to study the dynamics of spin glasses is ac susceptibility. The freezing temperature shifts as a function of ac frequency, which is analyzed in terms of the Vogel-Fulcher law and a critical scaling approach and enables the classification of cluster and canonical spin glasses [17]. In canonical spin glasses, the building blocks are individual moments whereas in cluster glasses, these moments act together and form clusters, which lead to a distinct dynamic behavior.

There are only a few reports on spin glass behavior in Heusler compounds, which is surprising considering their large number and variety of magnetic orders [11]. Spin glass behavior in Heusler compounds was previously observed in Cu<sub>2</sub>MnZ films (*Z* = Al, In, Sn) [18]. Despite having an ordinary Heusler composition, these films were amorphous. A reentrant spin glass state is quite common in Ni-Mn-based shape memory alloys [19–23]. These materials have a ferromagnetic cubic Heusler phase at high temperatures and transform to antiferromagnetic martensite upon cooling. Tetragonal martensite then undergoes a reentrant spin glass transition at low temperatures. The only reported cubic Heusler compound that exhibits spin glass behavior is Ru<sub>2-x</sub>Fe<sub>x</sub>CrSi with  $0.1 \leq x \leq 0.3$  [24,25]. Nevertheless, it is also a reentrant spin glass that is developed from antiferromagnetic order. To date, there have not been reports on spin glass states in half-Heusler compounds or on non-reentrant spin glass behavior in Heusler compounds. This study fills this gap in the literature by focusing on IrMnGa, which belongs to canonical spin glasses.

\*fecher@cpfs.mpg.de

## II. METHODS

### A. Single-crystal growth

In order to grow a single crystal of IrMnGa, a polycrystalline precursor was synthesized by conventional induction melting from stoichiometric amounts of pure elements. Crushed precursor pieces were placed in a tapered alumina crucible, which was sealed in a tantalum tube and then encapsulated in a quartz tube under argon atmosphere. The sample was heated to 1300 °C, held at this temperature for 10 h, then slowly cooled to 900 °C with a rate of 2 K/h, and finally quenched. The single crystallinity was confirmed by white-beam backscattering Laue x-ray diffraction at room temperature. Energy-dispersive x-ray spectroscopy (EDXS) was carried out and the analysis revealed an average composition of Ir<sub>31.3</sub>Mn<sub>31.9</sub>Ga<sub>36.8</sub>. Despite the small deviation from the stoichiometric composition, we refer to the sample as IrMnGa. The crystal was cut to a bar-shaped piece with dimensions of (3 × 1.5 × 0.5) mm<sup>3</sup> with the long side oriented in the [100] direction. This piece was used for all magnetic and transport measurements.

### B. Magnetic and transport measurements

The magnetization measurements were performed on an MPMS3 by Quantum Design. The ac susceptibility measurements were carried out on the same device with an alternating magnetic field of 0.5 mT for frequencies below 500 Hz and with 0.2 mT for frequencies above 500 Hz. The longitudinal and Hall resistivity were measured with a low-frequency ac current in five-point geometry (ACT option, PPMS9, Quantum Design). The Hall resistivity data were antisymmetrized with respect to the applied magnetic field whereas the longitudinal resistivity data were symmetrized. For the temperature-dependent Hall effect, two temperature sweeps were carried out, one with a positive and one with a negative field of the same magnitude. The data were subsequently antisymmetrized to subtract the contribution of the longitudinal resistivity. Heat capacity measurements were carried out on the same PPMS9 device with the heat capacity option.

### C. Diffraction and Rietveld refinement

The material for x-ray and neutron powder diffraction was synthesized by repeated induction melting from stoichiometric amounts of the pure elements with an overall weight loss of less than 1%. Subsequently, the material was homogenized for 14 days at 900 °C in argon atmosphere. The ingots were then crushed and ground to powder with a particle size smaller than 20 μm. Thereafter, the powder was annealed for one hour at 800 °C in vacuum to release stress. The powder neutron diffraction (PND) was conducted on the E6 diffractometer at HZB (Berlin, Germany). The powder was filled in a vanadium cylinder with 5.2 mm diameter. A monochromatic neutron beam with 2.430 Å wavelength was used for measurements at 2 K and 88 K. The powder x-ray diffraction (PXRD) was carried out on a STOE Stadi-P powder diffractometer with Mo K<sub>α</sub> radiation in transmission geometry. Both diffraction data were analyzed using the FullProf Rietveld refinement software package.

### D. Density functional theory

The electronic and magnetic structures of IrMnGa were calculated using SPRKKR [26,27] in the local spin density approximation (LSDA). In particular, the generalized gradient approximation of Perdew, Burke, and Ernzerhof [28] was used for the parametrization of the exchange correlation functional. The details of the calculations are found in Refs. [29,30]. Chemical and spin disorders were treated in the coherent potential approximation [31,32]. The basic crystal structure of IrMnGa is a disordered face-centered-cubic structure (prototype LiMgPdSn; *cF*16; *F* $\bar{4}3m$  No. 216 *dcb*a). The atoms are placed with the following occupations on the 4*a* to 4*d* Wyckoff positions of the cubic cell: 4*a* (Mn : Ga = 0.55 : 0.45), 4*b* (Ir : □ = 0.8 : 0.2), 4*c* (Mn : Ga = 0.45 : 0.55), 4*d* (Ir : □ = 0.2 : 0.8). The Schottky symbol (□) assigns the void. The calculations of the electronic structure and magnetic properties were performed for the lattice parameter *a* = 6.03 Å. Calculations were performed for ferromagnetic, ferrimagnetic, and disordered local moment states. The ferrimagnetic state was found from an initial antiferromagnetic setting of the spin of the Mn atoms in positions 4*a* and 4*c*. The disordered local moment state is sometimes seen as a prototype for a spin glass [33]. It was simulated by placing the same amount of Mn with spin up (↑) and spin down (↓) characters onto the 4*a* and 4*c* positions; e.g., one has on 4*a* the occupation Mn ↑: Mn ↓: Ga = 0.275 : 0.275 : 0.45. Both chemical disorder and disordered moments were treated on the basis of the coherent potential approximation.

## III. RESULTS

### A. X-ray diffraction

The atomic ordering was investigated in terms of powder x-ray diffraction and Rietveld refinement. There are two reports on IrMnGa and its structure in the literature: (i) Hames *et al.* [13] reported the first synthesis of the compound and noted its disordered *C*1<sub>*b*</sub> half-Heusler structure (prototype MgAgAs; *cF*12; *F* $\bar{4}3m$  No. 216 *cb*a) without specifying the type of disorder; (ii) Helmholtz *et al.* [12] carried out neutron diffraction and suggested a *C*1<sub>*b*</sub> structure with partial Ir-Mn disorder. Accordingly, Mn and Ir share 4*a* and 4*c* Wyckoff sites whereas Ga and the vacancy occupy the 4*b* and 4*d* positions.

In fact, the refined lattice parameter of 6.035 Å agrees well with the results of both studies [12,13]. Nevertheless, the calculated intensities for the Helmholtz model do not match the observed ones (*R*<sub>wp</sub> = 19.5%). Notably, there are no additional reflections compared to a fully ordered half-Heusler alloy. Hence, space group 216 is correct but the distribution of the elements on the four Wyckoff positions is different from the proposed one. The problem of chemical ordering in half-Heusler compounds involves distributing four species (three elements and one void) on four positions (4*a*, 4*b*, 4*c*, and 4*d*) [34]. Moreover, partial disorder with unequal site occupation of two or more species is also possible, illustrating the large parameter space. A practical first approach to determine the ordering in Heusler alloys is to inspect the intensity of the superlattice reflections (111) and (200) [35]. Suitable types of ordering may be identified by comparing

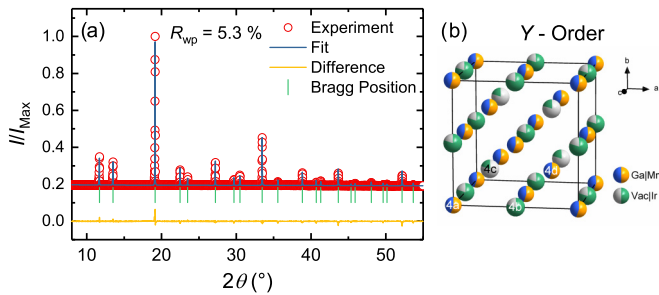


FIG. 1. Room temperature powder x-ray diffraction of IrMnGa. (a) Powder XRD pattern and Rietveld refinement assuming a  $Y$ -type crystal structure, as shown in (b).

the theoretical intensities of these two reflections for several models with the experimental results. The best fit for IrMnGa is obtained with  $Y$ -type order (prototype LiMgPdSn;  $cF16$ ;  $F43m$  No. 216  $dcb$ ;  $R_{wp} = 5.3\%$ ) as presented in Fig. 1(b). For this type of crystallographic order, Mn and Ga share the  $4a$  and  $4c$  positions whereas Ir and the void are distributed on  $4b$  and  $4d$  sites. Crucially, there is no complete intermixing but a preferred occupation as summarized in Table I. The model is plausible for two reasons. First, the Mn-Ga disorder is known from other Heusler compounds such as  $Ni_2MnGa$  [36]. Second, the largest atom Ir mixes with the void, which reduces local stresses.

### B. Neutron diffraction

In order to verify the proposed structure model, powder neutron diffraction was performed. Thereby, advantage is taken of the element's distinct scattering length for x rays and neutrons. The diffraction patterns at 2 K and 88 K with the corresponding Rietveld refinements are illustrated in Fig. 2. The number of available Bragg peaks within the measurement range is limited because of the high symmetry of space group 216 and the long neutron wavelength. Furthermore, Ir is a strong neutron absorber, which reduces the signal-to-noise ratio. Within these limitations, the  $Y$  model fits the experimental data well. Moreover, the obtained occupations, summarized in Table I, are consistent with those from the XRD refinement. Notably, the model proposed by Helmholtz *et al.* [12] also fits the PND data; however, it can be rejected because of

TABLE I. Summary of the refined site occupations from powder x-ray diffraction (PXRD) and powder neutron (PND) experiments. The model from Helmholtz *et al.* [12] is added for comparison. The Schottky symbol ( $\square$ ) assigns the void.

Wyckoff Position	Site Occupation (%)		
	This Work		
	PXRD	PND	Ref. [12]
$4a$ (000)	58 Mn + 42 Ga	55 Mn + 45 Ga	63 Ir + 37 Mn
$4b$ ( $\frac{1}{2} \frac{1}{2} \frac{1}{2}$ )	80 Ir + 20 $\square$	79 Ir + 21 $\square$	100 $\square$
$4c$ ( $\frac{1}{4} \frac{1}{4} \frac{1}{4}$ )	42 Mn + 58 Ga	45 Mn + 55 Ga	37 Ir + 63 Mn
$4d$ ( $\frac{3}{4} \frac{3}{4} \frac{3}{4}$ )	20 Ir + 80 $\square$	21 Ir + 79 $\square$	100 Ga

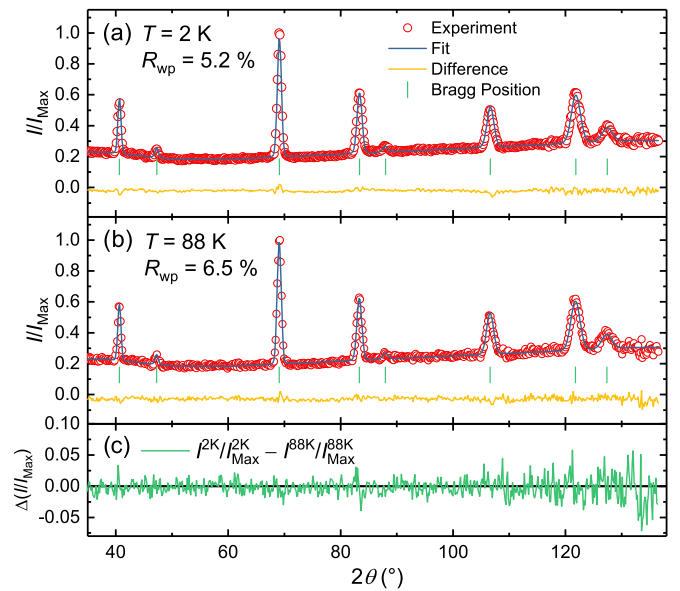


FIG. 2. Powder neutron diffraction at (a) 2 K and (b) 88 K. The blue lines are Rietveld fits assuming a  $Y$ -type structure. (c) Difference between the experimental patterns at 2 K and 88 K. Note the absence of magnetic Bragg peaks at low temperatures.

lack of agreement with the PXRD data. The derived  $R_{wp}$  coefficients indicate a good quality of the Rietveld refinement. The importance of the model lies in the fact that its physical consequences for the magnetism agree with the experimental observations as discussed in the next paragraph.

Since Mn is the only magnetic element in IrMnGa, the arrangement of Mn atoms entirely determines the magnetic properties of the compound. Moreover, the coupling of the Mn moments is highly sensitive to the distance to the next neighbors, which is a consequence of the oscillatory Ruderman-Kittel-Kasuya-Yoshida (RKKY) exchange. This exchange mechanism couples localized moments—such as those from Mn—via polarization of conduction electrons and can be either positive or negative depending on the distance between the moments. It is the dominant exchange interaction in Mn-based Heusler compounds. Prominent examples for this dependency are ferromagnetic shape memory alloys, where a slight distortion of the high-temperature austenite compared to the low-temperature martensite causes a transition from ferromagnetic to antiferromagnetic ordering [37,38]. The presented model of the  $Y$ -type disorder involves Mn on two positions and thereby implies a randomly varying distance to the nearest and next-nearest Mn neighbors. As a consequence, competing exchange interactions and frustration are expected.

As will be shown later, magnetization measurements reveal a magnetic phase transition around 74 K. However, a comparison of PND patterns at 88 K and 2 K shows neither additional Bragg peaks nor additional intensity on top of the peaks at low temperatures [Figs. 2(a) and 2(b)]. The absence of magnetic Bragg peaks indicates the absence of long-range magnetic order, which is in fact one characteristic of spin glasses [14–16,39]. This observation is also consistent with the proposed structure model because disorder and competing exchange interactions are required for the formation of a

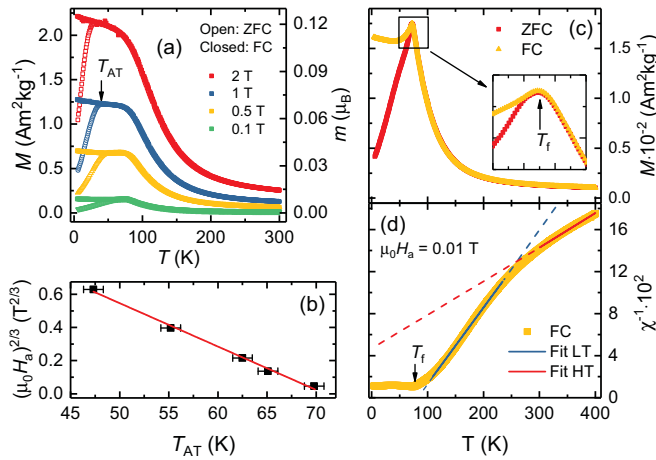


FIG. 3. Temperature-dependent magnetization. (a) Magnetization in different applied fields along [100]. Open symbols correspond to the zero-field-cooled (ZFC) and closed symbols to field-cooling (FC) branch. The temperature at which FC and ZFC branches meet is marked exemplarily by  $T_{AT}$ . (b) De Almeida–Thouless plot. (c) Temperature-dependent magnetization in 0.01 T. The freezing temperature at 74 K is marked by  $T_f$ . The inset displays a zoom to the region around the spin glass transition. (d) Inverse susceptibility. The straight lines correspond to a Curie–Weiss fit for high-temperature (HT) and low-temperature (LT) regime, respectively.

spin glass state and are both expected for  $Y$ -type chemical ordering.

Despite spin glasses missing long-range order, the presence of a short-range order should enhance diffuse scattering, which would cause intensity between atomic Bragg peaks. Generally, diffuse scattering is treated by investigating the difference in the neutron patterns above and below the spin glass freezing temperature. The difference between the patterns at 2 K and 88 K is plotted in Fig. 2(c). Apparently, the low signal-to-noise ratio due to the large neutron absorption cross section of Ir impedes the observation of an increased background. Nevertheless, we confirm the spin glass state at low temperatures in the following section by magnetization measurements.

### C. Magnetic properties

The temperature dependence of the magnetization is presented in Fig. 3(a). The zero-field-cooled (ZFC) branch agrees well with the literature [13] and appears like a broad antiferromagnetic transition. Unlike this, the field-cooling (FC) magnetization, which remains almost constant at low temperatures, is reminiscent of a ferromagnet. Notably, the irreversibility cannot be suppressed by applying moderately high magnetic fields. Such a pronounced bifurcation is typical for spin glasses. The spin glass character of the transition can be confirmed by investigating the temperature  $T_{AT}$ , where the irreversibility between FC and ZFC occurs. According to the de Almeida–Thouless relation,  $T_{AT}$  should shift to lower temperatures with higher magnetic fields and follow an  $H^{2/3}$  behavior in small fields [40]. Indeed, this relation holds true for the samples in this study as illustrated in Fig. 3(b).

In small magnetic fields, a distinct cusp of the magnetization is observed. The temperature at the maximum corre-

sponds to the freezing temperature  $T_f$  [Fig. 3(c)], which is higher than that in other spin glasses that commonly freeze below 30 K [14–16]. This is not surprising because  $T_f$  often depends linearly on the concentration of the magnetic atom [14] and IrMnGa contains 33% Mn, which is a higher concentration than for other spin glasses [14,39,41,42]. The Curie–Weiss behavior is illustrated in Fig. 3(d). Two temperature regimes are distinguished: (i) Above 300 K, the fit yields  $2.6 \mu_B$  per Mn atom; (ii) between 230 K and 110 K, the effective moment is reduced to  $1.8 \mu_B$ . The paramagnetic Curie temperature  $\theta_p$  for the high-temperature regime is determined as  $-134$  K, which suggests dominantly antiferromagnetic interactions in the system. The reduced effective moment at intermediate temperatures is occasionally observed in spin glass systems and attributed to a change of antiferromagnetic-like to ferromagnetic-like correlations [43–45]. Assuming only spin contribution ( $g = 2$ ) and an atomic moment of  $4 \mu_B$  ( $S = 2$ ), the expected effective paramagnetic moment is  $4.9 \mu_B$ , which is significantly higher than  $2.6 \mu_B$  derived for the high-temperature regime. Therefore, within this temperature range, the moments are not fully independent. This is also reflected in the small curvature of the inverse susceptibility in Fig. 3(d), which indicates that correlations are still present up to 400 K.

The effective paramagnetic moment from the Curie law can be compared with the site-specific moments from the electronic structure calculations. The magnetic properties from these calculations are summarized in Table II. The Mn moments on the  $4c$  sites are slightly larger than those at the  $4a$  sites owing to the different nearest-neighbor environment of those sites caused by the different occupation. Moreover, the disordered local moment calculations reveal the localized character of the  $d$  electrons at the Mn atoms. Notably, the moments are on the order of 3 to  $4 \mu_B$ , which is typical for Mn-containing Heusler compounds [11,46]. The size of the magnetic moments is independent of the assumed magnetic order as usual for localized magnetic moments. Independent of the type of magnetic order, the largest exchange coupling is found between the Mn atoms on  $4a$  and  $4c$  that are the nearest neighbors and it is on the order of 200 meV. The values in the disordered local moment state are between those of the ferromagnetic and ferrimagnetic states. A dominating role of the nearest-neighbor exchange integrals was also found in the calculations of other Heusler compounds that are suggested as spin glasses [47]. This is typical for short-range magnetic orders in such compounds.

Isothermal field-dependent magnetization measurements were carried out to study the spin glass state in more detail. The results are illustrated in Fig. 4(a). The magnetization does not reach saturation up to 7 T, which indicates antiferromagnetic interactions and the frustrated character of the system. Further, a hysteresis is observed below 50 K, whose coercivity reaches 1.1 T at 5 K [Fig. 4(b)]. The presence of seemingly hard magnetic properties of spin glasses is explained by random anisotropy [14,42]. Moreover, the observation of a remanence or coercivity unambiguously rules out simple antiferromagnetic ordering. Nevertheless, the ordered magnetic moment per formula unit is small with only  $0.25 \mu_B$  in 7 T at 5 K. This is understood considering the electronic structure calculations: although Mn atoms carry about  $4 \mu_B$ , they mainly—but not exclusively—couple

TABLE II. Properties of MnIrGa with ferromagnetic (fm) or ferrimagnetic (fim) order and in the disordered local moment (dlm) state. Magnetic moments ( $m$ ) are given in  $\mu_B$ . The exchange-coupling parameters  $J_{ij}$  are given in eV. Subscripts  $ij$  denote the interaction between the atoms on the two different sites  $4a$  and  $4c$ .

	$m_{\text{Mn}(4a)}$	$m_{\text{Mn}(4c)}$	$m_{\text{tot}}$	$J_{ac}$	$J_{aa}$	$J_{cc}$
fm	3.676	4.076	4.055	-0.242	-0.081	-0.019
fim	-3.616	3.972	0.552	0.181	-0.048	-0.017
dlm	$\pm 3.623$	$\pm 4.003$	0	$\pm 0.205$	$\pm 0.060$	$\pm 0.017$

antiferromagnetically, which leads to a small remaining net moment.

Another typical behavior of a spin glass is the presence of unidirectional anisotropy after field cooling [14,16,42,43]. Comparing hysteresis loops at 5 K after FC and ZFC indeed reveals the displacement of the FC loop [Fig. 4(b)]. This corresponds to the bifurcation already observed in the  $M(T)$  curves in Fig. 3(a). In the case of ZFC, the spins freeze collectively upon cooling through  $T_f$  without any preferred orientation. When switching on the field, the system minimizes its energy by aligning the spins with the externally applied field. However, due to the frustrated magnetic interactions, the system is trapped in a metastable state and only a few moments can actually align. This also leads to magnetic relaxation and memory effects as discussed in the next section. During FC, a preferred orientation is introduced and the system directly takes a configuration with more aligned spins upon cooling through  $T_f$ . This minimizes its energy and results in a higher net moment for the FC procedure, which is in fact observed in both the temperature- and field-dependent magnetization measurements.

There are two further phenomena that can cause loop shifts, namely exchange bias [6,48] and the minor-loop effect [6,49]. In exchange-bias systems, FC leads to a loop shift along the cooling-field direction. Importantly, the observed shift here is not only along the field but also along the magnetization axis so that exchange bias can be excluded. Minor loops occur when the material is not fully saturated before reversing the field. This can cause a hysteresis displacement along both axes. In fact, the detected FC loop

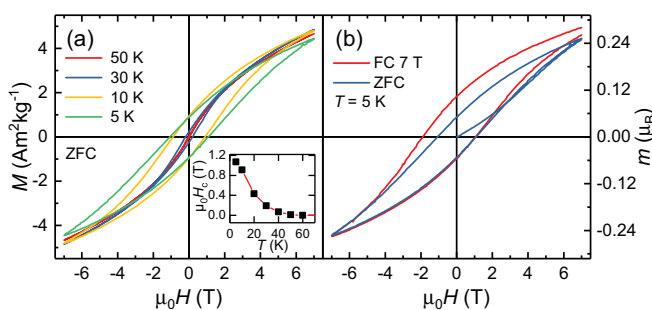


FIG. 4. Field-dependent magnetization. (a) Magnetization at different temperatures. The sample was zero-field cooled from above  $T_f$  and the field is applied along [100] direction. The inset depicts the coercivity as a function of temperature. (b) Comparing FC and ZFC hysteresis loops at 5 K. Characteristically, the FC loop is shifted along field and magnetization axes.

does not saturate and is not closed, which implies that it is a minor loop. However, it is almost closed and if the displacement originates from a minor-loop effect, then the ZFC curve should be shifted as well. The observed loop shifts are consequently attributed to the spin glass state in IrMnGa.

#### D. Magnetic relaxation

Similarly to other frustrated systems, spin glasses exhibit a pronounced temporal relaxation below  $T_f$  [14–16]. Therefore, the relaxation behavior was studied using the time-dependent magnetization measurements at various temperatures and applied magnetic fields. For this purpose, the sample was zero-field cooled from above  $T_f$  and subsequently a magnetic field was applied. The resulting time dependence  $M(t)$  is illustrated in Figs. 5(a) and 5(c). The magnetization increases with time, which is also denoted as the magnetic aftereffect. The curves follow a stretched exponential given by the Kohlrausch-Williams-Watts equation [50–52]:

$$M(t) = M_0 \{1 + a \exp[-(t/\tau)^b]\}. \quad (1)$$

The equation involves the characteristic relaxation time  $\tau$ , the shape parameter  $b$ , and the further fitting parameter  $a$ ,

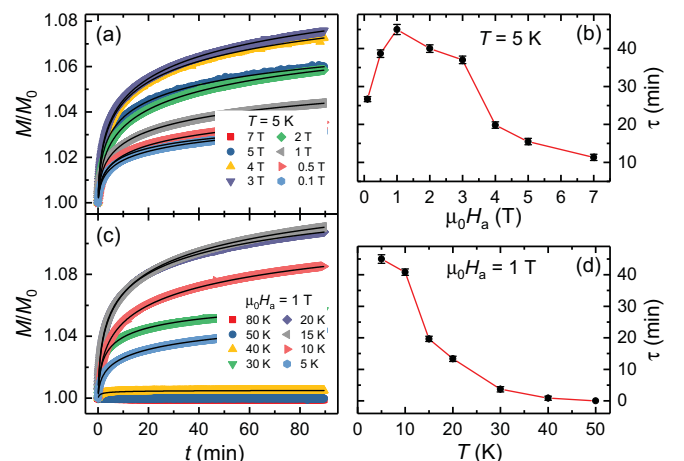


FIG. 5. Time-dependent magnetization. For all curves, the sample was first zero-field cooled from above  $T_f$  to the corresponding temperature and then the magnetic field was switched on. The magnetic field was applied along [100] direction. The black lines are fits with the Kohlrausch-Williams-Watts formula. (a) Relaxation at 5 K with various applied magnetic fields. (b) Extracted time constants from (a). (c) Relaxation at different temperatures in 1 T applied field. (d) Extracted time constants from (c).

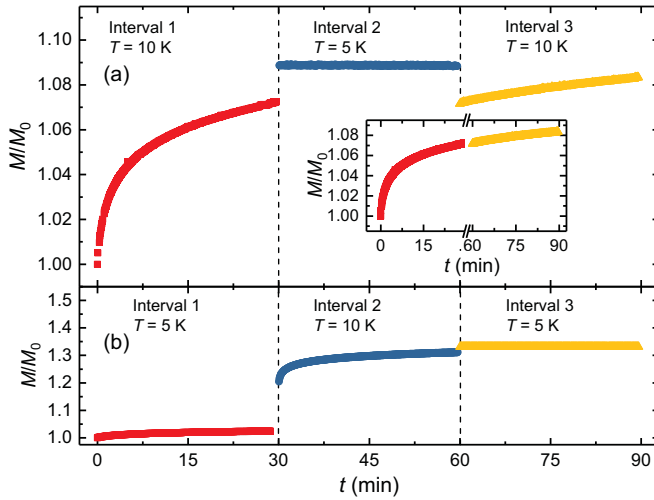


FIG. 6. Memory effect. The sample was first zero-field cooled from above  $T_f$  to the corresponding temperature and then a magnetic field of 1 T along [100] direction was switched on. (a) Relaxation at 10 K with intermediate cooling to 5 K. In the inset magnetization data from intervals 1 and 3 are merged. (b) Relaxation at 5 K with intermediate heating to 5 K. The systems respond asymmetrically to an intermediate temperature change.

which is related to the glassy component of magnetization. The extracted time constants  $\tau$  are on the order of minutes whereas the determined shape parameters  $b$  are between 0.21 and 0.49, which is normal for frustrated systems [22,53,54]. The influence of the applied field was studied at 5 K [Fig. 5(a)]. The corresponding time constant  $\tau$  goes through a maximum with a peak at a field of 1 T [Fig. 5(b)]. This can be understood since small fields lead to only partial alignment of the moments, so that already some aligned moments are sufficient. High fields instead align more moments but also exert a larger alignment force. Consequently, small and high fields should have a shorter time constant than intermediate fields, which is in fact observed. To study the temperature dependence of the relaxation, the applied field was fixed to 1 T [Fig. 5(c)]. The relaxation time is the highest at low temperatures [Fig. 5(d)] and decreases with increasing temperature. This reflects the reduction of energy barriers, which trap the system in its metastable state, at higher temperatures. Notably, the relaxation can be neglected when considering the magnetization curves, for example, for the comparison of ZFC and FC curves [Fig. 4(b)]. The time constants of approximately tens of minutes are significantly larger than the sweep rates ( $\sim 120$  mT/s) such that all data are equally unrelaxed.

The memory effect is another property of spin glasses [14,16,42]. In order to observe the effect, the sample was zero-field cooled from the paramagnetic state to 10 K and subsequently a magnetic field of 1 T was applied. Similarly to the relaxation experiments, the magnetization was measured as a function of time (interval 1). However, after 30 min, the temperature was quickly decreased to 5 K, then kept at this temperature for 30 more min (interval 2), and finally raised back to 10 K (interval 3). The result of this procedure is illustrated in Fig. 6(a). Fitting together the magnetization data from interval 1 and 3 reveals that

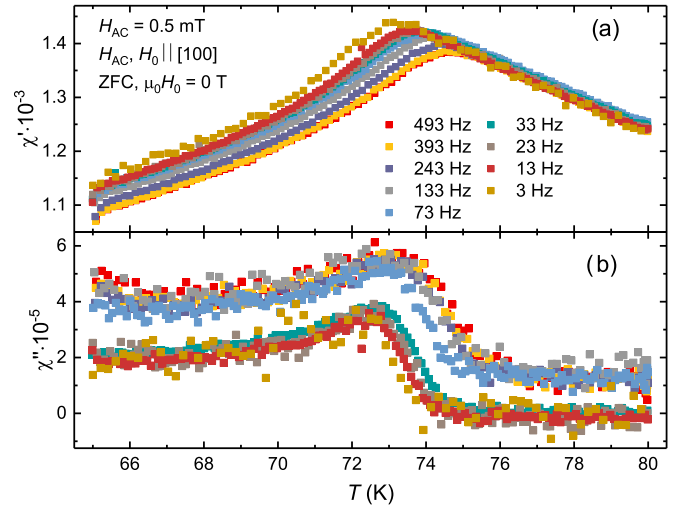


FIG. 7. Temperature dependency of the ac susceptibility around  $T_f$ . The sample was zero-field cooled and the ac magnetic field was applied along [100]. (a)  $\chi'$  with various frequencies. (b)  $\chi''$  with various frequencies.

both branches match as if no intermediate cooling has been carried out as well. The system “memorizes” its state from before the intermediate cooling and returns to this state after reheating. As presented in Fig. 6(b), an inverse-temperature protocol was carried out. The only difference from the previous procedure is intermediate heating instead of intermediate cooling. In this case, the system does not return to the magnetization from before intermediate heating.

The memory behavior can be described by two theoretical models, the droplet [55,56] and the hierarchical model [16,57]. According to the hierarchical model, there exists a multivalley free-energy landscape with several possible spin configurations at a particular temperature whereas the droplet model suggests only one distinct spin configuration. A major experimental difference is that the hierarchical model predicts the observation of the memory effect only for intermediate cooling. The droplet model predicts it for both temperature protocols. Since we only observe the memory effect for intermediate cooling, this supports the hierarchical model, which agrees well with other spin glass systems [44,45,58].

### E. The ac susceptibility

Measuring the ac susceptibility is the method of choice to investigate the dynamics of spin glasses. Originally, it was a sharp cusp in ac susceptibility at  $T_f$  that attracted attention to spin glasses in the early 1970s [59,60]. Indeed, a sharp peak is observed for the real part  $\chi'$  in Fig. 7(a). The corresponding  $T_f$  matches well with the dc freezing temperature, introduced in Fig. 3(c). Below  $T_f$ ,  $\chi'$  is smaller for higher frequencies whereas in the paramagnetic regime above  $T_f$ , all curves coincide.  $T_f$  shifts up for higher frequencies, which is a hallmark of spin glasses. In contrast, long-range-ordered ferro- or antiferromagnets only show such shifts at significantly higher frequencies in the MHz range [14]. Spin glasses can be classified using the Mydosh parameter, which measures the

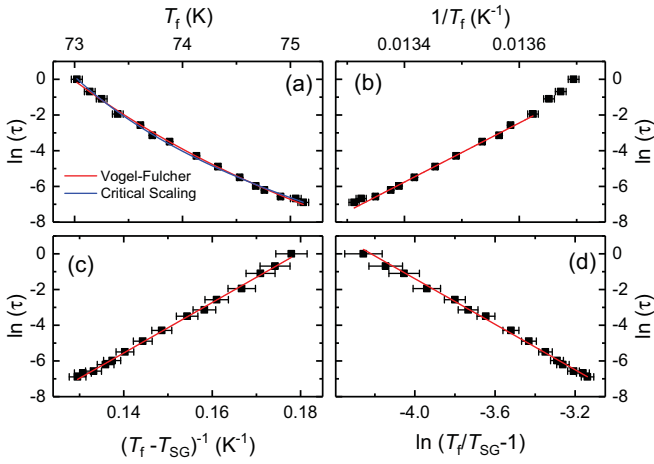


FIG. 8. Fitting the shift of  $T_f$ . (a) Relaxation time as a function of  $T_f$ . (b) Arrhenius plot. (c) Vogel-Fulcher plot. (d) Critical scaling plot. The Vogel-Fulcher law and the critical scaling approach both fit the shift equally well, but the Arrhenius law fails.

relative temperature shift per decade and is calculated by

$$K = \Delta T_f / (T_f \log_{10} \Delta f). \quad (2)$$

$K = 0.01$  is obtained for IrMnGa. This value is in the typical range of canonical spin glasses such as AuFe [61,62]. Moreover, this value is outside the range expected for superparamagnets and cluster glasses (0.1–0.28) [14]. The steplike increase of the imaginary part of the susceptibility  $\chi''$  around  $T_f$  is displayed in Fig. 7(b). The reason for the higher  $\chi''$  in the spin glass regime is the metastable and frustrated ground state, which causes irreversibility and thus enhances absorption.

There are three empirical laws to model the dependence of  $T_f$  on the frequency:

- (i) Arrhenius law:  $\tau = \tau_0 \exp(\frac{E_a}{k_B T_f})$ .
- (ii) Vogel-Fulcher law:  $\tau = \tau_0 \exp[\frac{E_a}{k_B(T_f - T_{SG})}]$ .
- (iii) Critical-scaling approach:  $\tau = \tau_0 [\frac{T_f}{T_{SG}} - 1]^{-z\nu}$ .

The relaxation time  $\tau$  corresponds to the inverse of the ac frequency whereas  $T_f$  is determined from the experiment. The fitting involves the characteristic spin relaxation time  $\tau_0$ , the activation energy  $E_a$ , the spin glass temperature  $T_{SG}$ , and the dynamical critical exponent  $z\nu$ .  $k_B$  is the Boltzmann constant.

Figure 8(b) shows that the Arrhenius law is not suitable to describe the shift in IrMnGa. First, it does not fit the whole frequency range. Second, and more importantly, the obtained parameters have unrealistic values ( $\tau_0 \approx 10^{-96}$  s,  $E_a/k_B \approx 16000$  K). Nonetheless, this also excludes superparamagnetism, which also causes a frequency dependence of  $T_f$  but follows the Arrhenius plot. Contrarily, the Vogel-Fulcher and critical-scaling approaches both yield a reasonable fit over the whole range of frequencies [Fig. 8(a)]. The determined spin relaxation time  $\tau_0$  is on the order of  $10^{-12}$  s and thus falls in the typical range for canonical spin glasses [14,42]. The same is true for the critical exponent  $z\nu \approx 6.2$ . The activation energy  $E_a/k_B$  of the Vogel-Fulcher law is related to the exchange interactions. It is often found that  $E_a/k_B \approx 2T_f$  [63], which is also consistent with our fit. All fitting parameters

TABLE III. Parameters obtained from the fitting of data shown in Fig. 8 with the Arrhenius, Vogel-Fulcher, and critical-scaling laws. Both Vogel-Fulcher and critical-scaling approaches indicate that IrMnGa belongs to the canonical spin glasses.

	Unit	Arrhenius	Vogel-Fulcher	Critical Scaling
$\tau_0$	s	$1 \times 10^{-96}$	$(1 \pm 0.5) \times 10^{-11}$	$(4 \pm 2) \times 10^{-12}$
$E_a/k_B$	K	$1.6 \times 10^4$	$141 \pm 42$	
$T_{SG}$	K		$67.4 \pm 0.1$	$72.0 \pm 0.1$
$z\nu$				$6.2 \pm 0.3$

are summarized in Table III. To conclude this analysis, both empirical laws indicate that IrMnGa belongs to the canonical spin glasses.

## F. Transport properties

The longitudinal resistivity  $\rho_{xx}$  is approximately  $300 \mu\Omega$  cm and decreases slightly upon warming [Fig. 9(a)]. The order of magnitude and the temperature behavior are typical for disordered metals in general and Heusler compounds in particular [64–67]. There is no feature in  $\rho_{xx}(T)$  at  $T_f$  for any of the applied fields because scattering of the conduction electrons is dominated by impurity scattering due to atomic disorder. Indeed, there is a contribution of magnetic spin disorder scattering but it is small and does not set in abruptly at  $T_f$ . It changes gradually with temperature because local correlations are already present above the collective freezing at  $T_f$  [14] (compare with the discussion of the Curie-Weiss plot).  $\rho_{xx}$  shows only a weak field dependence that completely vanishes above 100 K. The minor impact of an applied field is also seen in field-dependent measurements, illustrated in Fig. 9(b). The magnetoresistance in  $\mu_0 H = 9$  T,

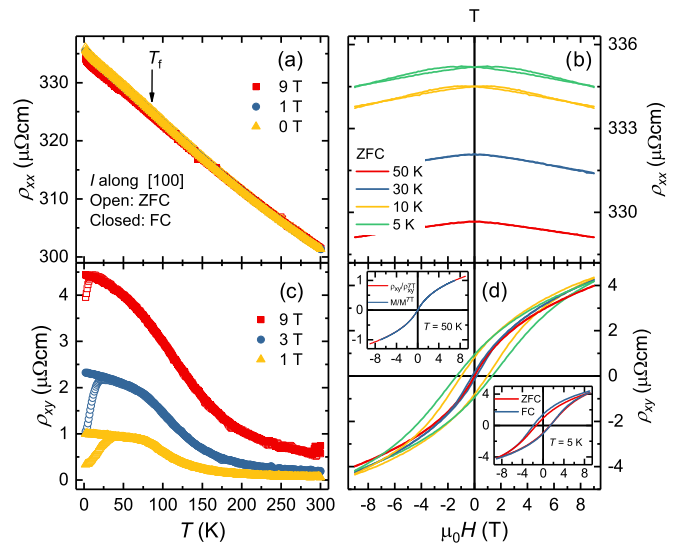


FIG. 9. Electrical transport. The current was directed along [100] and the sample was zero-field cooled. (a) Temperature-dependent longitudinal resistivity. (b) Temperature-dependent Hall resistivity. (c) Field-dependent longitudinal resistivity. (d) Field-dependent Hall resistivity. The left inset displays normalized Hall and magnetization data at 50 K. The right inset illustrates the comparison of FC and ZFC Hall resistivity at 5 K.

$T = 5$  K is slightly negative ( $-0.2\%$ ). Notably, there is a small deviation for branches of ascending and descending fields at low temperatures. The effect occurs simultaneously with coercivity and is even weaker than the magnetoresistance ( $0.05\%$ ).

The temperature-dependent Hall resistivity  $\rho_{xy}(T)$  [Fig. 9(c)] resembles the course of the magnetization [Fig. 3(a)]. The bifurcation between zero-field-cooled and field-cooling branches is still present up to 9 T, which indicates that spin glass transition cannot be suppressed by this applied field. The temperature  $T_{AT}$ , where the irreversibility between FC and ZFC branches occurs, matches for both magnetization and resistivity data. This finding agrees with the earlier reports of the anomalous Hall effect in spin glasses [68,69], where the origin of the anomalous Hall effect was attributed to the frustrated noncoplanar spin structure. The similarities with the magnetization also become clear for the field-dependent Hall resistivity [Fig. 9(d)].  $\rho_{xy}(H)$  directly follows the  $M(H)$  curves so that the contribution of the ordinary Hall can be neglected. To confirm this, Hall and magnetization data at 50 K were normalized to their value at 7 T and plotted in the left inset. Indeed, there is no additional increase in  $\rho_{xy}$ , which originates from a sizable ordinary Hall effect. The vanishingly small ordinary Hall effect was also observed in other metallic canonical spin glasses [69,70]. Moreover, it is even possible to shift the loop similarly to Fig. 4(b).

### G. Specific heat

In contrast to long-range-ordered systems such as ferromagnets, which exhibit a  $\lambda$ -shaped anomaly at their ordering temperature, spin glasses show no feature of the specific heat at their freezing temperature [14,42]. The reason is that the magnetic entropy is majorly freezing out above  $T_f$  due to correlations between the spins, which occur already at much higher temperatures [14]. Indeed, no anomaly or shoulder is observed in temperature-dependent specific-heat measurements at  $T_f$  [Fig. 10(a)]. The specific heat around room temperature attains a value close to that of the Dulong-Petit rule. Furthermore, the influence of an applied field is negligible. Figure 10(b) illustrates  $C_p/T$  as a function of  $T^2$  for temperatures below 10 K. The straight line corresponds to a fit to equation  $C_p = \gamma T + \beta T^3$ , where the first term is associated with the contribution of conduction electrons and the second one with the contribution of phonons. The fit yields a Sommerfeld coefficient  $\gamma$  of 16 mJ/(mol K<sup>2</sup>) and a  $\beta$  of 0.33 mJ/(mol K<sup>4</sup>), which implies a Debye temperature  $\Theta_D$  of 262 K.  $\beta$  is thus significantly smaller than the observed value for some cluster glasses [71,72]. This indicates that IrMnGa is a spin but not a cluster glass.

## IV. SUMMARY

This study investigated the half-Heusler compound IrMnGa, which crystallizes in the normal half-Heusler space group 216 but is highly disordered. The previously suggested model for the chemical disorder does not fit the XRD data. Considering both x-ray and neutron diffraction, we proposed

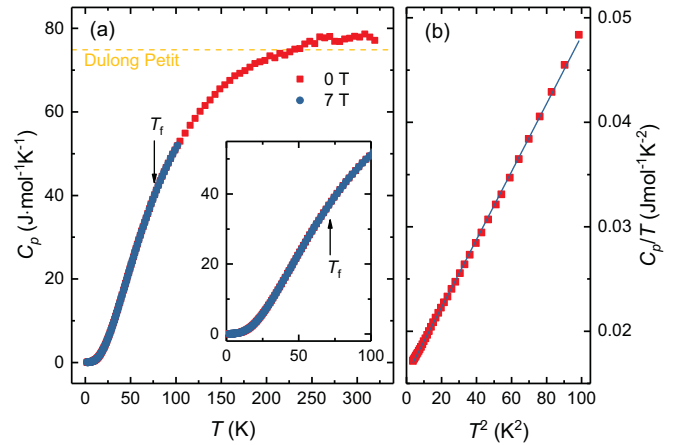


FIG. 10. Heat capacity. The data were collected while cooling. (a) Temperature-dependent heat capacity measurements for 0 and 7 T. The inset presents a zoom-in plot of low temperatures. There is no  $\lambda$ -shaped anomaly at  $T_f$  (marked by an arrow). The yellow line corresponds to the value expected by the Dulong-Petit rule. (b)  $C_p/T$  as a function of  $T^2$  for temperatures below 10 K.

the  $Y$ -type disorder. Mn and Ga share the  $4a$  and  $4c$  positions, whereas Ir is distributed on the  $4b$  and  $4d$  positions. The absence of magnetic Bragg peaks in the neutron diffraction experiment indicates the absence of long-range magnetic ordering. In fact, magnetic measurements demonstrate spin glass behavior below the freezing temperature  $T_f = 74$  K:

- (i) The magnetization exhibits a bifurcation below  $T_f$  between zero-field-cooled and field-cooling branches.
- (ii) A hysteresis with coercivity up to 1.1 T is observed at low temperatures.
- (iii) Hysteresis loops may be shifted along both field and magnetization axes by field cooling.
- (v) A sharp cusp of the ac susceptibility at  $T_f$  is observed.

Moreover, the frustrated character of the system is confirmed by the pronounced magnetic aftereffect and the memory effect. The shift of  $T_f$  with the variation of ac frequency can be modeled using the Vogel-Fulcher law and the critical-scaling approach. Both methods indicate that IrMnGa belongs to the class of canonical spin glasses ( $\tau_0 \approx 10^{-12}$  s). The longitudinal resistivity remains almost constant upon warming due to the large degree of disorder. The Hall resistivity directly follows magnetization and is entirely dominated by the anomalous Hall contribution, whereas the contribution of the ordinary Hall effect can be neglected. The spin glass character is further confirmed by the absence of an anomaly in the specific heat at  $T_f$ . This study demonstrates that IrMnGa is a half-Heusler spin glass. This adds a further magnetic functionality to this highly tunable material class.

## ACKNOWLEDGMENTS

The authors thank Christian Blum (IFW, Dresden) for carrying out powder x-ray diffraction, Oliver Stockert (MPI-CPFS) for organizing the neutron measurements, and Ralf Koban (MPI-CPFS) for help with the transport measurements. The project was funded by the DFG Priority Program SPP 2137 ‘‘Skyrmionics’’.

- [1] A. K. Nayak, J. E. Fischer, Y. Sun, B. Yan, J. Karel, A. C. Komarek, C. Shekhar, N. Kumar, W. Schnelle, J. Kübler *et al.*, *Sci. Adv.* **2**, e1501870 (2016).
- [2] S. Nakatsuji, N. Kiyohara, and T. Higo, *Nature (London)* **527**, 212 (2015).
- [3] K. G. Rana, O. Meshcheriakova, J. Kübler, B. Ernst, J. Karel, R. Hillebrand, E. Pippel, P. Werner, A. K. Nayak, and C. Felser, *New J. Phys.* **18**, 085007 (2016).
- [4] A. Neubauer, C. Pfleiderer, B. Binz, A. Rosch, R. Ritz, P. G. Niklowitz, and P. Böni, *Phys. Rev. Lett.* **102**, 186602 (2009).
- [5] N. Kanazawa, Y. Onose, T. Arima, D. Okuyama, K. Ohoyama, S. Wakimoto, K. Kakurai, S. Ishiwata, and Y. Tokura, *Phys. Rev. Lett.* **106**, 156603 (2011).
- [6] J. M. D. Coey, *Magnetism and Magnetic Materials* (Cambridge University Press, Cambridge, UK, 2010).
- [7] O. Meshcheriakova, S. Chadov, A. K. Nayak, U. K. Rößler, J. Kübler, G. André, A. A. Tsirlin, J. Kiss, S. Hausdorf, A. Kalache *et al.*, *Phys. Rev. Lett.* **113**, 087203 (2014).
- [8] S. Singh, S. W. DeSouza, J. Nayak, E. Suard, L. Chapon, A. Senyshyn, V. Petricek, Y. Skourski, M. Nicklas, C. Felser *et al.*, *Nat. Commun.* **7**, 12671 (2016).
- [9] A. K. Nayak, V. Kumar, T. Ma, P. Werner, E. Pippel, R. Sahoo, F. Damay, U. K. Rößler, C. Felser, and S. S. P. Parkin, *Nature (London)* **548**, 561 (2017).
- [10] A. Regnat, A. Bauer, A. Senyshyn, M. Meven, K. Hradil, P. Jorba, K. Nemkovski, B. Pedersen, R. Georgii, S. Gottlieb-Schönmeier *et al.*, *Phys. Rev. Mater.* **2**, 054413 (2018).
- [11] T. Graf, C. Felser, and S. S. P. Parkin, *Prog. Solid State Chem.* **39**, 1 (2011).
- [12] R. B. Helmholtz, R. A. de Groot, F. M. Mueller, P. G. van Engen, and K. H. J. Buschow, *J. Magn. Magn. Mater.* **43**, 249 (1984).
- [13] F. A. Hames and J. Crangle, *J. Appl. Phys.* **42**, 1336 (1971).
- [14] J. A. Mydosh, *Spin Glasses: An Experimental Introduction* (Taylor & Francis Ltd., London, 1993).
- [15] J. A. Mydosh, *Rep. Prog. Phys.* **78**, 052501 (2015).
- [16] H. Kawamura and T. Taniguchi, in *Handbook of Magnetic Materials*, edited by K. H. J. Buschow (Elsevier, Amsterdam, Netherlands, 2015), Vol. 24, Chap. 1, pp. 1–137.
- [17] J. Souletie and J. L. Tholence, *Phys. Rev. B* **32**, 516 (1985).
- [18] L. Krusin-Elbaum, A. P. Malozemoff, and R. C. Taylor, *Phys. Rev. B* **27**, 562 (1983).
- [19] S. Morito, T. Kakeshita, K. Hirata, and K. Otsuka, *Acta Mater.* **46**, 5377 (1998).
- [20] S. Chatterjee, S. Giri, S. K. De, and S. Majumdar, *Phys. Rev. B* **79**, 092410 (2009).
- [21] L. Ma, W. Wang, J. Lu, J. Li, C. Zhen, D. Hou, and G. Wu, *Appl. Phys. Lett.* **99**, 182507 (2011).
- [22] A. K. Nayak, K. G. Suresh, and A. K. Nigam, *J. Phys.: Condens. Matter* **23**, 416004 (2011).
- [23] J. K. Sun, C. Jing, C. Q. Liu, Y. S. Huang, X. D. Sun, Y. L. Zhang, M. F. Ye, and D. M. Deng, *J. Supercond. Novel Magn.* **1** (2018), <https://link.springer.com/article/10.1007%2Fs10948-018-4899-x>.
- [24] M. Hiroi, T. Rokkaku, S. Mizutani, S. Fujii, and S. Ishida, *J. Phys.: Conf. Ser.* **150**, 042058 (2009).
- [25] M. Hiroi, H. Ko, S. Nakashima, I. Shigeta, M. Ito, H. Manaka, and N. Terada, *J. Phys.: Conf. Ser.* **400**, 032020 (2012).
- [26] H. Ebert, in *Electronic Structure and Physical Properties of Solids: The Use of the LMT0 Method*, Lecture Notes in Physics, Vol. 535, edited by H. Dreyse (Springer-Verlag, Berlin, 1999), p. 191.
- [27] H. Ebert, D. Ködderitzsch, and J. Minar, *Rep. Prog. Phys.* **74**, 096501 (2011).
- [28] J. P. Perdew, K. Burke, and M. Ernzerhof, *Phys. Rev. Lett.* **77**, 3865 (1996).
- [29] H. C. Kandpal, G. H. Fecher, and C. Felser, *J. Phys. D: Appl. Phys.* **40**, 1507 (2007).
- [30] G. H. Fecher, S. Chadov, and C. Felser, in *Spintronics*, edited by C. Felser and G. H. Fecher (Springer-Verlag, Dordrecht, 2013), Chap. 7, p. 115.
- [31] P. Soven, *Phys. Rev.* **156**, 809 (1967).
- [32] A. J. Pindor, W. J. Staunton, G. M. Stocks, and H. Winter, *J. Phys. F: Met. Phys.* **13**, 979 (1983).
- [33] H. Akai and P. H. Dederichs, *Phys. Rev. B* **47**, 8739 (1993).
- [34] G. E. Bacon and J. S. Plant, *J. Phys. F* **1**, 524 (1971).
- [35] P. J. Webster, *Contemp. Phys.* **10**, 559 (1969).
- [36] V. V. Khovailo, T. Takagi, A. N. Vasilev, H. Miki, M. Matsumoto, and R. Kainuma, *Phys. Status Solidi* **183**, R1 (2001).
- [37] S. Singh, J. Bednarcik, S. R. Barman, C. Felser, and D. Pandey, *Phys. Rev. B* **92**, 054112 (2015).
- [38] S. Esakki Muthu, N. V. Rama Rao, M. Manivel Raja, S. Arumugam, K. Matsubayasi, and Y. Uwatoko, *J. Appl. Phys.* **110**, 083902 (2011).
- [39] H. Maletta and W. Felsch, *Phys. Rev. B* **20**, 1245 (1979).
- [40] J. R. L. de Almeida and D. J. Thouless, *J. Phys. A: Math. Gen.* **11**, 983 (1978).
- [41] V. Cannella and J. A. Mydosh, *AIP Conf. Proc.* **10**, 785 (1973).
- [42] K. Binder and A. P. Young, *Rev. Mod. Phys.* **58**, 801 (1986).
- [43] R. Rodriguez, A. Fernandez, A. Isalgue, J. Rodriguez, A. Labrata, J. Tejada, and X. Obradors, *J. Phys. C* **18**, L401 (1985).
- [44] S. Kundu, T. Dey, A. V. Mahajan, and N. Büttgen, [arXiv:1807.05612](https://arxiv.org/abs/1807.05612).
- [45] T. Chakrabarty, A. V. Mahajan, and S. Kundu, *J. Phys.: Condens. Matter* **26**, 405601 (2014).
- [46] J. Kübler, A. R. Williams, and C. B. Sommers, *Phys. Rev. B* **28**, 1745 (1983).
- [47] P. Entel, M. E. Gruner, D. Comtesse, V. V. Sokolovskiy, and V. D. Buchelnikov, *Phys. Status Solidi B* **251**, 2135 (2014).
- [48] J. Nogués and I. K. Schuller, *J. Magn. Magn. Mater.* **192**, 203 (1999).
- [49] J. Geshev, *Appl. Phys. Lett.* **93**, 162515 (2008).
- [50] A. K. Nayak, C. Shekhar, J. Winterlik, A. Gupta, and C. Felser, *Appl. Phys. Lett.* **100**, 152404 (2012).
- [51] F. Alvarez, A. Alegria, and J. Colmenero, *Phys. Rev. B* **44**, 7306 (1991).
- [52] G. Bayreuther, P. Bruno, G. Lugert, and C. Turtur, *Phys. Rev. B* **40**, 7399 (1989).
- [53] J. C. Phillips, *Rep. Prog. Phys.* **59**, 1133 (1996).
- [54] R. V. Chamberlin, G. Mozurkewich, and R. Orbach, *Phys. Rev. Lett.* **52**, 867 (1984).
- [55] D. S. Fisher and D. A. Huse, *Phys. Rev. B* **38**, 373 (1988).
- [56] W. L. McMillan, *J. Phys. C* **17**, 3179 (1984).
- [57] V. S. Dotsenko, *J. Phys. C* **18**, 6023 (1985).
- [58] S. Pakhira, C. Mazumdar, R. Ranganathan, S. Giri, and M. Avdeev, *Phys. Rev. B* **94**, 104414 (2016).

- [59] J. I. Budnick, V. Cannella, and T. J. Burch, *AIP Conf. Proc.* **18**, 307 (1974).
- [60] V. Cannella and J. A. Mydosh, *Phys. Rev. B* **6**, 4220 (1972).
- [61] C. A. M. Mulder, A. J. van Duynveldt, and J. A. Mydosh, *Phys. Rev. B* **23**, 1384 (1981).
- [62] F. Holtzberg, J. L. Tholence, H. Godfrin, and R. Tournier, *J. Appl. Phys.* **50**, 1717 (1979).
- [63] S. Mukherjee, A. Garg, and R. Gupta, *Appl. Phys. Lett.* **100**, 112904 (2012).
- [64] M. Kaveh and N. F. Mott, *J. Phys. C* **15**, L707 (1982).
- [65] C.-S. Lue and Y.-K. Kuo, *J. Appl. Phys.* **96**, 2681 (2004).
- [66] L. Bainsla, M. M. Raja, A. K. Nigam, B. S. D. Varaprasad, Y. K. Takahashi, K. G. Suresh, and K. Hono, *J. Phys. D* **48**, 125002 (2015).
- [67] Y. V. Kudryavtsev, Y. P. Lee, Y. J. Yoo, M. S. Seo, J. M. Kim, J. S. Hwang, J. Dubowik, K. W. Kim, E. H. Choi, and O. Prokhnenko, *Eur. Phys. J. B* **85**, 19 (2012).
- [68] P. Pureur, F. W. Fabris, J. Schaf, and I. A. Campbell, *Europhys. Lett.* **67**, 123 (2004).
- [69] T. Taniguchi, K. Yamanaka, H. Sumioka, T. Yamazaki, Y. Tabata, and S. Kawarazaki, *Phys. Rev. Lett.* **93**, 246605 (2004).
- [70] F. Wolff-Fabris, P. Pureur, J. Schaf, V. Vieira, and I. A. Campbell, *Physica B (Amsterdam)* **403**, 1373 (2008).
- [71] V. K. Anand, D. T. Adroja, and A. D. Hillier, *Phys. Rev. B* **85**, 014418 (2012).
- [72] J. Liu, Y. Mudryk, J. D. Zou, V. K. Pecharsky, and K. A. Gschneidner Jr., *J. Alloys Compd.* **600**, 101 (2014).